Low Temperatures Reduce Shallow Defect Energies and Interfacial Recombination Losses in Triple-Cation Lead-Halide Perovskites

Guus J. W. Aalbers,[1] Simon V. Quiroz Monnens,[1] S. Mihály Calis,[1] Willemijn H. M. Remmerswaal,[1] Martijn M. Wienk,[1] and René A. J. Janssen[1,2,*]

[1]*Materials to Optoelectronic Devices & Institute for Complex Molecular Systems, Eindhoven University of Technology, P.O. Box 513, 5600 MB Eindhoven, The Netherlands*
[2]*Dutch Institute for Fundamental Energy Research, De Zaale 20, 5612 AJ Eindhoven, The Netherlands*

(Received 6 March 2026; revised 9 June 2026; accepted 12 June 2026; published 8 July 2026)

Understanding the origin and mechanisms of defect-induced voltage losses and recombination in metal-halide perovskites aids in the development of new strategies to achieve higher solar cell efficiencies. Photoluminescence (PL) spectroscopy provides insight into charge recombination at defects in the perovskite and at interfaces with passivation and electron transport layers. Measuring the time-resolved PL as a function of temperature for a triple-cation mixed-halide perovskite (CsFAMA) reveals that the PL decay is dominated by shallow defects and that lowering the temperature changes the trap-energy landscape, making the shallow defects shallower until they vanish into the conduction or valence bands at 90 K. Depositing fullerene (C_{60}) on top of the CsFAMA perovskite induces significant nonradiative recombination losses at room temperature, which can largely be reduced by applying interfacial passivation. Interestingly, cooling to 90 K makes the charge-recombination dynamics almost identical for CsFAMA and CsFAMA/C_{60} films, irrespective of interfacial passivation treatments. At such low temperatures, nonradiative recombination losses become less dominant because interfacial recombination velocities are reduced. The results provide new insight into shallow defects and recombination losses in CsFAMA perovskites and help to better understand the effect of surface treatments on shallow-defect properties.

DOI: 10.1103/jzjm-xw3v

I. INTRODUCTION

Metal-halide perovskite solar cells (PSCs) are promising candidates for single- and multijunction applications, attributed to their excellent optoelectronic properties. Currently, nonradiative voltage losses are the primary reason limiting PSCs from achieving high open-circuit voltages (V_{OC}), which are critical for further improving the efficiency. Such nonradiative losses are typically induced by defective electronic states (traps) in the semiconductor layer, at grain boundaries, or at interfaces with adjacent charge transport layers (CTLs) and are often mediated via interstitials and vacancies [1,2]. Understanding the origin and mechanisms of voltage losses and recombination processes can aid in developing new strategies to achieve higher efficiencies.

In PSCs, the recombination of charge carriers typically occurs via radiative or defect-assisted Shockley-Read-Hall (SRH) mechanisms [3]. SRH recombination takes place via defect states that are either within the bandgap (deep) or close to the valence band (VB) or conduction band (CB). The deep defects are often considered detrimental to solar cell efficiency [4,5]. In contrast, shallow defects in perovskite semiconductors have low formation energies [6] and are often assumed to have a negligible impact on V_{OC} losses because trapped charge carriers can be thermally excited into the CB or VB [7,8]. However, recent work shows that for PSCs, it is, in fact, the shallow defects that dominate recombination and limit device efficiency [9]. Time-resolved photoluminescence (tr-PL) allows one to study the temporal carrier decay and provides insight into the dominant recombination mechanism. For most lead-halide perovskites, the tr-PL decay follows a power-law behavior at high carrier densities [9,10]. With sufficiently long SRH lifetimes for deep defects, the PL decay will be dominated by radiative recombination and nonradiative SRH recombination via shallow defects. These two mechanisms are almost indistinguishable from each other and result in comparable tr-PL. Only for SRH recombination via deep traps does the PL decay follow a monoexponential behavior at low carrier densities [10].

Layers adjacent to the perovskite film, such as CTLs, can also induce nonradiative recombination losses [11–13].

*Contact author: r.a.j.janssen@tue.nl

For example, fullerene C_{60}, often used as an electron transport layer (ETL), quenches the PL when in contact with the perovskite due to strong nonradiative losses [1,11]. To reduce nonradiative charge recombination at the perovskite/C_{60} interface, postdeposition surface treatments can be applied to passivate the perovskite layer and reduce the losses induced at this interface. For example, perovskite top-surface treatments using lithium fluoride (LiF) [14,15], choline chloride (CCl) [16,17], or propane-1,3-diammonium iodide [18] have effectively reduced the nonradiative recombination losses at the perovskite/C_{60} interface to a significant extent. Interestingly, treating the neat perovskite with CCl or LiF has no significant effect on the nonradiative voltage losses [11]; only when it is combined with a fullerene layer on top is its impact observed. This interfacial passivation might be attributed to the concept that these materials spatially separate the perovskite from the C_{60} layer and act as a tunnel barrier for electron transport [1,11,19]. However, these surface treatments might still affect shallow-defect properties while having minimal effect on the total V_{OC} losses [20,21].

Because shallow defects dominate charge recombination in metal-halide perovskites, understanding and controlling such defects is important for reducing nonradiative losses. Shallow-defect properties can be modified using perovskite bulk additives [22,23] or top surface treatments [9] and can impact PSC efficiency. Until now, the influence of perovskite surface treatments and CTLs on the properties of shallow defects in perovskites has not been explored. This motivated us to study the shallow-defect properties in triple-cation lead-halide perovskite films with passivation and electron transport layers on top. By measuring tr-PL, we find that the PL decay is dominated by shallow defects and that lowering the temperature changes the trap-energy landscape, making the shallow defects shallower until they vanish into the conduction or valence bands at 90 K. This result is corroborated by an increase in PL quantum yield and is explained by noting that the shallow defects are intrinsic to the triple-cation lead-halide perovskite and are formed through a thermally activated process. Depositing CCl, C_{60}, or a combination of both on top of the triple-cation lead-halide perovskite can induce significant nonradiative recombination losses at room temperature, but cooling to 90 K makes the charge-recombination dynamics almost identical across all treatments. At these low temperatures, nonradiative recombination losses become less dominant because interfacial recombination velocities are reduced. The results provide new insights into shallow defects and recombination losses in triple-cation lead-halide perovskites and enable a better understanding of the effect of surface treatments on shallow-defect properties.

II. RESULTS AND DISCUSSION

A. Neat triple-cation lead-halide perovskite films

To study the behavior of shallow defects, metal-halide triple-cation mixed-halide perovskite films were fabricated using a nominal composition of $Cs_{0.05}(FA_{0.83}MA_{0.17})_{0.95}Pb(I_{0.83}Br_{0.17})_3$, hereafter referred to as CsFAMA, on glass substrates functionalized with 1,6-hexylenediphosphonic acid (HDPA). HDPA minimizes the nonradiative losses induced by the substrate/CsFAMA interface and allows us to study a neat CsFAMA perovskite film with low inherent nonradiative voltage losses [24]. First, absolute steady-state PL (ss-PL) was measured to determine inherent nonradiative voltage losses due to defects in the neat CsFAMA perovskite film [Fig. 1(a)]. An ss-PL emission peak centered on 1.63 eV showed a high photon flux, which can be related to a quasi-Fermi level splitting (ΔE_F) of 1223 ± 9 meV via Planck's generalized radiation law (see Experimental Section in Supplemental Material, [25]). At open circuit, the quasi-Fermi level splitting is equal to the voltage of a solar cell under ideal conditions, and hence, for a film without contacts, ΔE_F is also referred to as the implied V_{OC}. The measured ΔE_F of 1223 meV is 119 meV below and equivalent to 91% of the radiative voltage limit (ΔV_{OC}^{rad}) of 1342 meV for the CsFAMA perovskite with a bandgap of 1.63 eV [5]. The ΔE_F showed minimal changes (< 10 meV) during 15 min of 1-Sun equivalent illumination, indicating good photostability and no detectable light-induced changes (Fig. S1 in Supplemental Material [25]). Nevertheless, defects still limit the CsFAMA perovskite film from achieving a higher ΔE_F and therefore impact the PL emission.

To study the behavior of charge-carrier recombination in neat CsFAMA films leading to nonradiative losses, tr-PL was measured using an intensified gated charge-coupled device camera, which enables measurement of the PL decay over a high dynamic range of ≈7.5 orders of magnitude. Figure 1(b) reveals that the normalized tr-PL emission ($\phi_{tr\text{-}PL}$) exhibits a power-law behavior with time ($\phi_{tr\text{-}PL} \propto t^{-\alpha}$) for $10^{-7} < t < 10^{-5}$ s with $\alpha \approx 2.75$. While long PL lifetimes have been associated with a variety of photophysical processes such as an indirect bandgap [29], dynamic defect tolerance [30], photon recycling [31], persistent photoluminescence [32], and memory effects [33], the appearance of a power-law decay at high carrier densities has consistently been explained to originate from shallow defects dominating the time-dependent PL [9,10].

The tr-PL decay can be converted into a carrier-density-dependent decay time (τ_{diff}), which is defined for high-level injection as [34]

$$\tau_{diff} = \left(-\frac{\mathrm{d}\,\ln\left[\phi_{tr\text{-}PL}(t)\right]}{2\mathrm{d}t} \right)^{-1}. \quad (1)$$

When τ_{diff} is plotted against $\Delta E_F(t,T)$, it is defined as

$$\Delta E_F(t,T) = \Delta E_F^{max}(T) + \frac{k_B T}{q} \ln\left[\phi_{tr\text{-}PL}(t,T)\right], \quad (2)$$

where

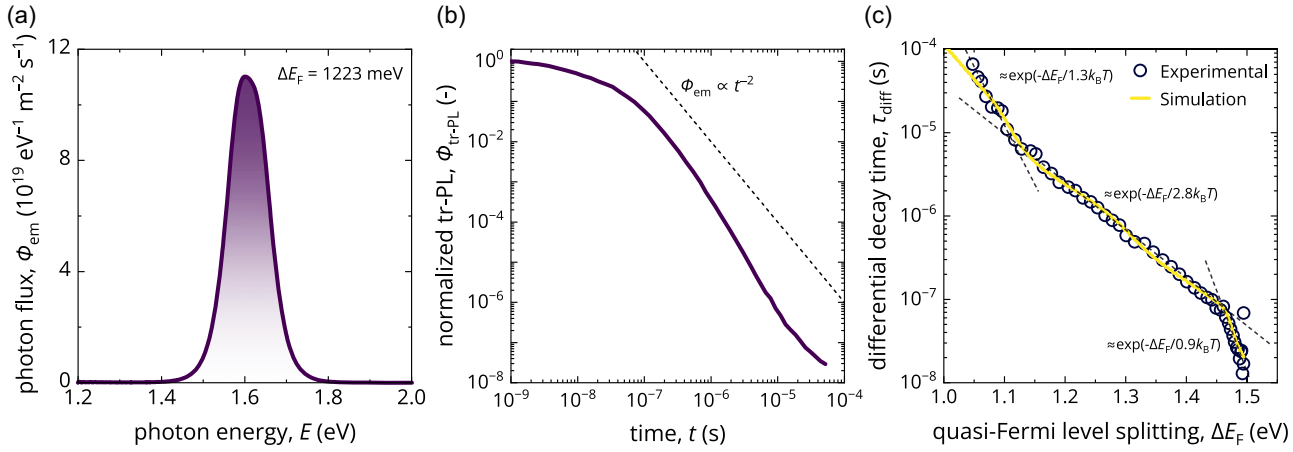

FIG 1. (a) Absolute steady-state PL (ss-PL) spectrum and (b) time-resolved PL (tr-PL) trace of a glass/HDPA/CsFAMA perovskite film. The dashed line represents a power-law decay, $\phi_{tr\text{-}PL} \propto t^{-2}$, expected for an intrinsic semiconductor [10]. (c) Carrier-density-dependent differential decay time (τ_{diff}) versus quasi-Fermi level splitting (ΔE_F) of neat glass/HDPA/CsFAMA film, where the blue circles represent the experimental data and the yellow solid line is the simulation. For tr-PL, the film was illuminated from the active (CsFAMA) side. Dashed lines are a guide to the eye to show slope factor θ.

$$\Delta E_F^{max}(T) = \frac{k_B T}{q} \ln\left(\frac{\Delta n^2}{n_i^2(T)}\right), \tag{3}$$

and k_B is the Boltzmann constant, T the temperature, q the elementary charge, Δn the average initial carrier concentration, and n_i the intrinsic carrier concentration (assumed to be 8×10^4 cm^{-3} for CsFAMA at room temperature) [35]. The differential decay time changes continuously at each ΔE_F with a varying slope of $0.9 \leq \theta \leq 2.8$, following $\tau_{diff} \propto \exp(-\Delta E_F/\theta k_B T)$ [Fig. 1(c)]. The continuously changing τ_{diff} and slope are not consistent with a single-exponent power-law behavior and also imply that assigning a single carrier decay time obtained from fitting exponential functions can be highly misleading, as the decay time changes over orders of magnitude depending on the excitation density and laser repetition rate [9,10]. Such long and changing decay times indicate that the tr-PL is limited by shallow defects, resulting in detectable long decay times of up to 70 μs at room temperature [9]. Deep-defect-assisted SRH recombination behavior is not visible from the tr-PL, as this would result in a constant τ_{diff} for all ΔE_F [34]. SRH recombination from deep defects might still be present and limit the achievable ΔE_F of the CsFAMA perovskite layer, but the corresponding SRH decay times must be (significantly) longer than 70 μs. Illumination from the active (CsFAMA perovskite) or glass side did not affect the shape of the decay time, but the initial carrier concentration after the laser pulse was marginally higher from the glass side because of a difference in reflectivity (Fig. S2 in Supplemental Material [25]). While the intensity of the laser pulse during tr-PL measurements affects the normalized PL intensity versus time decay, the carrier-density-dependent decay time is identical, regardless of the laser intensity (Fig. S3 in Supplemental Material [25]) [34]. Fitting τ_{diff} using a coupled rate equation assuming three defects with variable trap depths shows good agreement with the experimental data [Fig. 1(c)]. Details on the numerical model and the fitting parameters can be found in Note S1 in Supplemental Material [25]. Since the CsFAMA perovskite is considered an intrinsic semiconductor [36], the fitting cannot distinguish between donor-like and acceptor-like defects, and here we assume the defects to be of acceptor type, close to the CB. In the modeling, we do not account for possible equilibrium between excitons and free electrons and holes, because for the low exciton binding energy of CsFAMA (E_B = 16–21 meV [37]), the equilibrium dynamics is orders of magnitude faster than the radiative decay [38].

Measuring the PL as a function of temperature allows for studying thermally activated processes and characterizing the defects that dominate nonradiative charge recombination. When reducing the temperature from 300 to 90 K, the ss-PL spectrum of a neat CsFAMA film narrows from a full width at half maximum of 90 to 38 meV and shows a small (8 meV) redshift (Fig. S4 in Supplemental Material [25]), while presenting a 22-fold increase in the PL quantum yield (Q_e^{PL}) [Fig. 2(a)]. X-ray diffraction revealed that metal-halide perovskites similar to CsFAMA exhibit phase changes in the temperature range between 300 and 90 K, in particular a cubic to tetragonal (α-β) phase transition at 300–270 K and a second to a γ-phase around 180 K [39–41]. However, in agreement with results for similar triple-cation mixed-halide perovskites [37,41], the ss-PL spectra of CsFAMA only change gradually with temperature, without discontinuities or new peaks [Figs. S4(b) and S4(c) in Supplemental Material [25]]. This suggests a minimal impact of the phase transitions on the PL properties. The enhanced $Q_e^{PL} = R_{rad}/(R_{rad} + R_{SRH})$ results from a higher radiative recombination rate

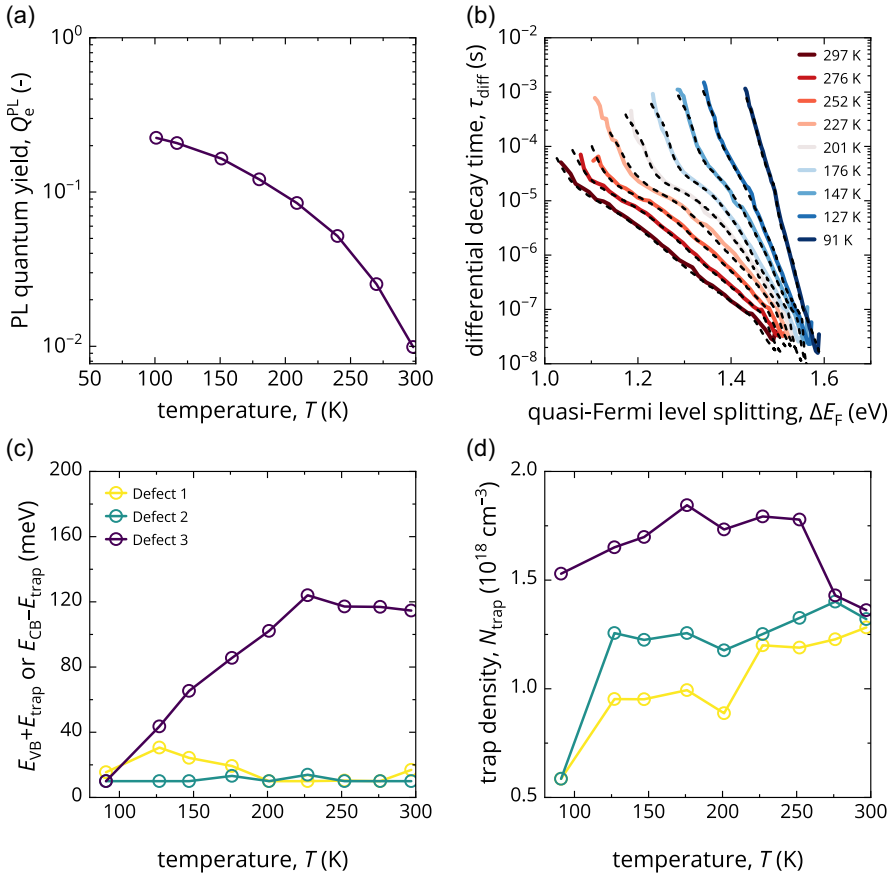

FIG 2. (a) Temperature-dependent measured PL quantum yield (Q_e^{PL}) of a CsFAMA perovskite film on HDPA-functionalized glass. (b) Carrier-density-dependent differential decay time (τ_{diff}) versus quasi-Fermi level splitting (ΔE_F) of a CsFAMA perovskite film on HDPA-functionalized glass at different temperatures (solid lines) and fitting of differential decay time (dashed lines) using coupled rate equations assuming three shallow defects. The film was excited from the glass side. (c) Trap energy (E_{trap}) relative to the CB or VB of the perovskite and (d) trap density (N_{trap}) from fitting the τ_{diff} of (b).

(R_{rad}) via $R_{rad}(T)=k_{rad}(T)np$ [26,40,42,43], a decrease in the rate of SRH recombination (R_{SRH}) [44], or a combination of both. $R_{rad}(T)$ enhances sevenfold when the CsFAMA perovskite is cooled from 300 K to 130 K, as determined from the PL intensity ($\phi_{tr\text{-}PL}(T, t = 0)$) after laser excitation (Fig. S5 in Supplemental Material [25]). Hence, the enhanced Q_e^{PL} at 130 K is a combination of increasing R_{rad} and a reducing R_{SRH} of 3 times. As a consequence, ΔE_F improved from 1235 meV at 300 K to 1532 meV at 100 K when determined from the enhanced Q_e^{PL}, assuming an absorption of unity above the bandgap as explained in the Experimental Section (see Supplemental Material [25]). These values of ΔE_F correspond to 92% and 99% of the detailed-balance limits at these temperatures, respectively (Fig. S6 in Supplemental Material [25]). The gain in ΔE_F seen between 300 and 100 K is a combination of the enhanced Q_e^{PL} and a gain in thermodynamic efficiency according to the detailed-balance theory.

The tr-PL traces of a neat CsFAMA film measured in the same temperature range show that PL emission can still be measured at approximately 1 ms after the laser pulse at 90 K (Figs. S7 and S8 in Supplemental Material [25]). To convert the tr-PL at below room temperature into a carrier-density decay time, ΔE_F must be defined at each temperature. Right after the laser pulse, the photogenerated carrier-density results in an initial ΔE_F equal to $\Delta E_F^{max}(T)$ [Eq. (3)] which depends on the thermal voltage and on the intrinsic carrier concentration, which can be calculated using

$$n_i^2(T) = N_C N_V \ln\left(\frac{-E_g}{k_B T}\right), \tag{4}$$

where E_g is the optical bandgap of the perovskite and N_C and N_V are the CB and VB density of states, respectively.

Figure 2(b) shows the differential decay time of the tr-PL traces at temperatures from 300 to 90 K. The shape of the tr-PL decay gradually changes from a power-law-like behavior at 300 K to a more monoexponential, SRH-related behavior at approximately 230 K, for which a constant τ_{diff} would be expected. At temperatures below 230 K, the SRH-like behavior slowly disappears, and the tr-PL returns to a power-law behavior at 90 K, where the

PL decay behaves virtually as a pure radiative emitter without contributions from defects (Fig. S9 in Supplemental Material [25]). The tr-PL traces were independent of the thermal history of the sample and appeared identical at a given temperature, irrespective of whether they were recorded during cooling of the CsFAMA perovskite to 90 K or when reheating to 300 K (Fig. S10 in Supplemental Material [25]). This confirms that the sample does not change during an 8-h experiment and that any phase transition is reversible.

As described by Eq. (2), ΔE_F increases at lower temperatures for identical initial carrier concentrations (Δn), resulting in a change in the slope of τ_{diff} versus ΔE_F at lower temperatures. As a result, at constant ΔE_F, the differential decay time is longer at lower temperatures. This is not due to the increased k_{rad} at reduced temperatures (Figs. S5 and S11 in Supplemental Material [25]), but τ_{diff} increases for a fixed ΔE_F at lower temperatures because the carrier density corresponding to that Fermi-level splitting is reduced. From simulations, we find similar behavior between 300 and 100 K when assuming that no SRH recombination is present [Figs. S12(a) and S12(b) in Supplemental Material [25]], and that pure power-law behavior ($\phi_{tr\text{-}PL} \propto t^{-\alpha}$) results in ever-increasing differential decay times when the carrier density is reduced. Only when SRH-type recombination is present will the decay time reach a constant value, regardless of the temperature [Fig. S12(c) in Supplemental Material [25]]. From the experimental data, the decay time increases as the temperature is reduced, reaching values of ≈1 ms and showing a more defect-free character similar to that of a perovskite with only radiative recombination (Fig. S9 in Supplemental Material [25]). At intermediate temperatures, between 230 and 175 K, the decay time versus ΔE_F has a different shape, and there is a notable change in slope around $\tau_{diff} \approx 5 \times 10^{-5}$ s [Fig. 2(b)].

The results suggest that the energetic landscape of traps is shifting with temperature. To address the reproducibility of these findings, the tr-PL traces and decay times of another set of samples are shown in Figs. S13(a) and S13(b) in Supplemental Material [25]). Similar tr-PL behavior with comparable long decay times can be observed for all temperatures, demonstrating the reproducibility of these results.

Due to the soft ionic nature of perovskites, their defect densities depend on the temperature of the perovskite and its corresponding formation energy [45,46]. To gain a better understanding of the changing trap-energy landscape of the CsFAMA film at various temperatures, the decay times were fitted using coupled rate equations (Note S1 in Supplemental Material [25]). Following work from Yuan *et al*. [9], we assume three shallow defects close to the CB or VB, as these defects can be donor- or acceptor-type and the fitting cannot distinguish between the two because the perovskite is considered to be an intrinsic semiconductor [36]. Global fitting of the differential decay times, assuming identical defect properties (i.e., temperature-independent trap densities (N_t) and energies (E_t)) across all temperatures, resulted in inaccurate fits (Fig. S14 in Supplemental Material [25]).

This finding suggests that the trap-energy landscape is dynamic and changes when the CsFAMA perovskite is cooled from 300 to 90 K. In contrast, when fitting with temperature-dependent defect properties, good fits were obtained at each temperature when assuming a minimum of three defects [Fig. 2(b)]. In the model, we enforce a minimal trap depth of 10 meV to prevent unphysical fitting results. Figures 2(c) and 2(d) show the shallow trap energy (depth) and trap density versus temperature. At room temperature, the trap energy (E_{trap}) distribution can be described with three shallow traps with energies of 17, 10, and 115 meV relative to the CB or VB. Interestingly, lowering the temperature results in the three defects becoming shallower. At ≈275 K, the first (17 meV) defect reaches the 10-meV minimal depth, and below ≈225 K, the deepest trap (115 meV) slowly becomes shallower until it also disappears into the band at ≈100 K [Fig. 2(c)]. This corroborates the finding that the CsFAMA decay time at 90 K follows almost a radiative-only charge recombination behavior, free of shallow defects (Fig. S9 in Supplemental Material [25]). In the 125–90 K region, the thermal energy ($k_B T$) is close to the minimal trap depth (10 meV) used in the model. To compensate for the inability to lower the trap energy, the fitting procedure lowers the shallow trap defect density [Fig. 2(d)]. We cannot exclude the possibility that defect (SRH) characteristics appear at decay times beyond ≈1 ms, but this was experimentally inaccessible due to the detection limit of the setup. In addition, at 100 K, the detrapping rate (e_n) from a shallow trap back to the bands is also slightly lowered (Fig. S15 in Supplemental Material [25]), as this is a thermally activated process, filling all shallow traps, which in turn, enhances radiative band-to-band emission as the nonradiative hole capture rate (β_p) also slightly reduces with temperature [9].

The trap density (N_{trap}) determined from the fitting remains fairly constant around $0.5\text{–}1.75 \times 10^{18}$ cm^{-3} for all three defects over the temperature range studied [Fig. 2(d)]. For a defect with a given formation energy, it is expected that the defect density will be reduced at lower temperatures [45,46]. However, when the defects become shallower at temperatures below 300 K, their formation energy decreases, which would increase the defect density. These counteracting effects can explain the similar defect densities across the temperature range studied.

The results presented in this section show that as the CsFAMA perovskite film cools, the energetic trap landscape changes, and its shallow traps become shallower. Consequently, the effects of shallow defects on the PL lifetime decrease.

B. CsFAMA perovskite with passivation and electron transport layers

To investigate the effect of interface-passivation treatments and the deposition of an ETL on the shallow-defect properties, CCl, C_{60}, and CCl/C_{60} were deposited on the top surface of CsFAMA films, and their tr-PL traces were measured at room temperature. For the CsFAMA film with CCl on top, a very similar τ_{diff} was found as for the neat film for ΔE_F between 1.3 and 1.5 eV, showing similar recombination behavior [Fig. 3(a)]. Only at $\Delta E_F < 1.3$ eV, where nonradiative recombination dominates, is the decay time for the CCl-treated film slightly lower compared to the neat film. Fitting of the decay time shows identical shallow trap densities and energies for the neat and CCl-treated CsFAMA films (Tables S1 and S2 in Supplemental Material [25]), with only a marginally reduced electron capture and emission rate resulting in a small difference in τ_{diff} for $1.1 < \Delta E_F < 1.3$ eV. From absolute ss-PL on the same films, no significant change in ΔE_F (1223 ± 9 meV versus 1226 ± 9 meV) was measured, suggesting a minimal impact of CCl on the nonradiative voltage losses (Fig. S16 in Supplemental Material [25]).

When C_{60} is deposited on top of the CsFAMA film, the decay time becomes significantly shorter across all ΔE_F due to enhanced nonradiative recombination [Fig. 3(a)], also evident from absolute ss-PL; the steady-state ΔE_F is reduced by about 100 to 1128 ± 7 meV (Fig. S16 in Supplemental Material [25]). The shortening of the decay time is due to fast electron transfer from CsFAMA to C_{60} followed by nonradiative charge recombination across the interface [47,48]. Alongside these carrier quenching channels, C_{60} might also introduce additional (deep) defect states [49,50], resulting in further quenching of the tr-PL decay time. Following the procedure of Lee *et al.* [26], the decay time at room temperature of the CsFAMA/C_{60} bilayer was fitted, assuming that C_{60} does not alter the defect properties of the CsFAMA film, i.e., the defect energy and density remained identical to a neat CsFAMA layer. In this model, only charge exchange and across-interface recombination pathways were introduced upon C_{60} deposition (see Note S2 in Supplemental Material for details [25]). From the fitting, an electron transfer rate (k_{et}), electron back transfer rate (k_{ebt}), and an interfacial recombination rate (R_{rec}) can be determined (Table S3 in Supplemental Material [25]). Such charge extraction and subsequent nonradiative interfacial recombination can significantly reduce the PL decay time of the CsFAMA/C_{60} bilayer and we find values that are comparable to those reported in the literature [47]. To get a sense of how lossy this CsFAMA/C_{60} interface is, we calculate a time-averaged effective interface carrier loss velocity ($\langle S_{eff} \rangle$) from the rate constants extracted from the fitting as a figure of merit to showcase how many carriers are lost at the interface due to both extraction and interfacial recombination (see Note S3 in Supplemental Material [25]). When C_{60} is deposited on top of a CsFAMA film, it induces a total $\langle S_{eff} \rangle$ of ≈5524 cm s^{-1} at room temperature, which is lower than values reported before for C_{60} [51]. Out of this $\langle S_{eff} \rangle$, ≈1731 cm s^{-1} is due to an across-interface recombination velocity (S_{int}) and ≈3793 cm s^{-1} is due to a charge-exchange velocity (S_{exc}) from CsFAMA to C_{60}. This demonstrates that the significant interfacial losses at the CsFAMA/C_{60} interface during tr-PL measurements are mainly due to rapid electron extraction from CsFAMA to C_{60}. By passivation strategies, the interfacial recombination losses can be reduced. Note that for efficient PSCs, the

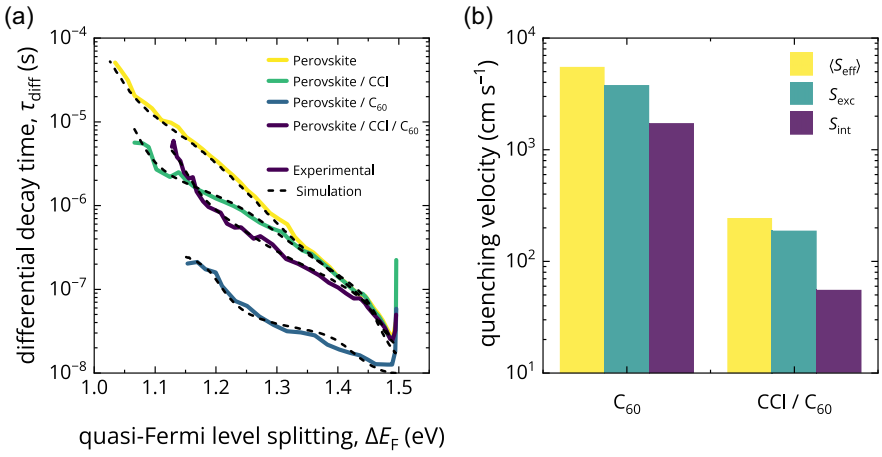

FIG 3. (a) Carrier-density-dependent differential decay time (τ_{diff}) versus quasi-Fermi level splitting (ΔE_F) of glass/HDPA/CsFAMA, glass/HDPA//CsFAMA/C_{60}, and glass/HDPA//CsFAMA/CCl/C_{60} (solid lines) and their corresponding simulation of a coupled rate equation (dashed lines, see Note S2 in Supplemental Material [25]). For tr-PL, the film was excited from the glass side. (b) Time-averaged effective interface carrier loss velocity ($\langle S_{eff} \rangle$), exchange velocity (S_{exc}), and across-interface recombination velocity (S_{int}) for glass/HDPA//CsFAMA/C_{60} and glass/HDPA//CsFAMA/CCl/C_{60} extracted from the fits in (a). For details, see Note S3 in Supplemental Material [25].

S_{exc} should be as high as possible to ensure good charge extraction, resulting in a high short-circuit current density and fill factor [52,53].

Passivation of the CsFAMA top surface with CCl before depositing C_{60} (CsFAMA/CCl/C_{60}) greatly enhances the decay time compared to that of the CsFAMA/C_{60} film combination [Fig. 3(a)], along with a substantial recovery of ΔE_F from 1128 ± 7 to 1178 ± 8 meV (Fig. S16 in Supplemental Material [25]) as determined from ss-PL, showing that the nonradiative recombination at the CsFAMA/C_{60} interface is greatly reduced by the CCl interlayer. Interface carrier loss velocities were determined by fitting the tr-PL decay using the method described above. The CsFAMA/CCl/C_{60} has a reduced $\langle S_{eff} \rangle$ by almost 23 times to $\approx$245 cm s^{-1}. This lowering is mainly due to the reduced charge-exchange velocity ($S_{exc} = 189$ cm s^{-1}) because CCl acts as a barrier for electron transfer and back transfer, lowering the number of transferred electrons in the C_{60} (Table S3 in Supplemental Material [25]), in turn limiting the amount of interfacial recombination ($S_{int} = 56$ cm s^{-1}). Both the reduced interfacial recombination velocity and the lower exchange velocity result in lower charge quenching and, therefore, a longer retained carrier concentration in the CsFAMA perovskite during tr-PL experiments.

Next, the decay times of the surface-treated CsFAMA films were measured between 300 and 90 K (Fig. S17 in Supplemental Material [25]). We first look at the CCl-treated CsFAMA films, where the decay time is similar to that of the neat film and becomes longer when the temperature is reduced, reaching $\tau_{diff} \approx 1$ ms at 90 K. Using the fitting methodology of coupled rate equations, the shallow-defect properties are determined for a CsFAMA/CCl film at various temperatures (Fig. S18 in Supplemental Material [25]). As for the neat CsFAMA film, the shallow defect density remains relatively constant between 0.9 and 2×10^{18} cm^{-3} across the measured temperature range. These densities are comparable to those of the neat CsFAMA and show that CCl treatment does not significantly alter the shallow defect density. Cooling the CsFAMA/CCl film from 300 to 100 K also results in a changing trap-energy landscape, with three traps becoming shallower until they vanish into the bands around 100 K, making CsFAMA more defect-free. This thermally activated behavior of the shallow defects is almost identical between the neat and CCl-treated films, demonstrating the limiting effect of CCl on reducing shallow traps.

When C_{60} is directly deposited on the CsFAMA film, the initially short decay times ($< 10^{-7}$ s) gradually increase over the entire ΔE_F range as the temperature is reduced, approaching a measured 10^{-4} s close to 90 K [Fig. S17(b) in Supplemental Material [25]]. In addition, at 90 K, the slope becomes more akin to the recombination kinetics of a neat perovskite film, suggesting a reduction in charge extraction and interface recombination at the CsFAMA/C_{60} interface. At 90 K, the decay times of a CsFAMA/C_{60} film and a neat film are very similar, i.e., the shapes of the τ_{diff} versus ΔE_F curves are similar. This implies that when the temperature is lowered, all films exhibit less nonradiative recombination character and enhanced radiative emission. Interestingly, the longest measurable decay time, i.e., until the PL signal disappears below the detection limit of the setup, of the CsFAMA/C_{60} film at 90 K is only $\approx$40 μs, whereas for the neat film it is $\approx$1 ms. This suggests that there is still a loss of charge carriers, probably due to the fast electron transfer from CsFAMA to C_{60} with $k_{et} \approx 10^7$ s^{-1} at these temperatures, coupled with reduced electron back transfer rates of $k_{ebt} \approx 50$ s^{-1}, as this is a thermally activated process (Fig. S19 in Supplemental Material [25]). For the CsFAMA films with CCl/C_{60} on top, τ_{diff} becomes longer across all ΔE_F values when the temperature is lowered and again reaches $\approx$1 ms at 90 K. This demonstrates that when the temperature is lowered, the decay times become more similar to those of a semiconductor with limited defects and a low effective carrier loss velocity. The CsFAMA/CCl/C_{60} film also shows the most prominent change in τ_{diff} slope around 10^{-6} s, probably due to a rapid reduction in R_{rec} around 230 K (Fig. S20 in Supplemental Material [25]).

Extending the analysis of the CsFAMA/ETL bilayer to below room temperature using the tr-PL fitting procedure described in Note S3 in Supplemental Material [25] allows for the disentangling of the contributions to the effective interface carrier loss velocities (Fig. S21 in Supplemental Material [25]). For a CsFAMA/C_{60} stack, the $\langle S_{eff} \rangle$ reduces from $\approx$5524 cm s^{-1} at room temperature to $\approx$422 cm s^{-1} at 90 K [Fig. 4(a)], showing a significant reduction in carrier quenching. S_{int} decreases by 3 orders of magnitude when cooling from 300 to 90 K, from $\approx$1731 to $\approx$2 cm s^{-1}. The reduction in S_{int} is a consequence of a stark drop of R_{rec} [Fig. S19(c) in Supplemental Material], which suggests that interfacial recombination is thermally activated as a consequence of an interfacial trap state or band bending at the CsFAMA/C_{60} interface as proposed previously [1,54]. S_{exc} reduces almost an order of magnitude from $\approx$3793 to $\approx$420 cm s^{-1} across the temperature range, primarily starting from 150 K. This reduction in charge-exchange velocity might be due to reduced charge mobility at cryogenic temperatures. These results demonstrate that the carrier quenching at the CsFAMA/C_{60} interface becomes benign and results in lower nonradiative recombination, boosting radiative efficiency.

CsFAMA perovskite films with CCl/C_{60} on top show a significantly lower interface carrier loss velocity across the entire temperature range of 300–130 K, demonstrating a reduction in nonradiative voltage losses, as seen from the ss-PL ΔE_F (Fig. S16 in Supplemental Material [25]). The large reduction in $\langle S_{eff} \rangle$ compared to the CsFAMA/C_{60} stack without CCl treatment is due to a lower interface

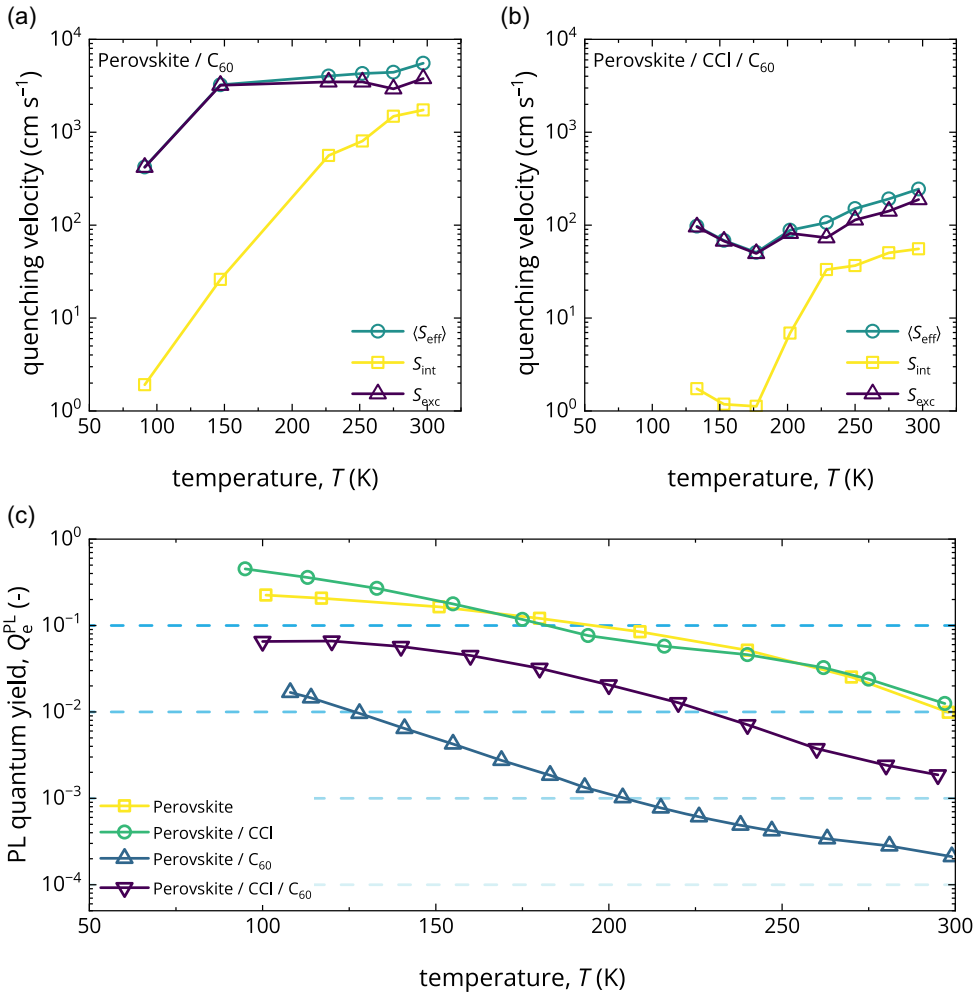

FIG 4. (a),(b) Time-averaged effective interface carrier loss velocity ($\langle S_{\mathrm{eff}} \rangle$), exchange velocity ($S_{\mathrm{exc}}$), and across-interface recombination velocity (S_{int}) of glass/HDPA/CsFAMA/C_{60} (a) and glass/HDPA/CsFAMA/CCl/C_{60} (b) at various temperatures determined from fitting the temperature-dependent tr-PL traces. (c) Temperature-dependent measured PL quantum yield (Q_e^{PL}) of glass/HDPA/CsFAMA, glass/HDPA/CsFAMA/CCl, glass/HDPA/CsFAMA/C_{60}, and glass/HDPA/CsFAMA/CCl/C_{60} (symbols). Dashed blue lines are reference lines assuming different PL quantum yields.

recombination velocity S_{int}, which reduces from ≈56 to ≈1.7 cm s^{-1} when cooled from 300 to 130 K [Fig. 4(b)]. Moreover, the charge-exchange velocity S_{exc} also reduces from ≈189 to ≈96 cm s^{-1} at 130 K. Both quenching velocities become smaller at 130 K, showing that even the CCl-treated CsFAMA bilayers become less lossy and result in lower nonradiative recombination. We emphasize that the model for CsFAMA/C_{60} bilayers, described in Note S2 in Supplemental Material [25], assumes an unaltered CsFAMA interface when adjacent to C_{60}, i.e., without additional defects. The only carrier quenching channels induced by the CsFAMA/C_{60} bilayer are related to charge transfer and interfacial recombination. The addition of a C_{60}-induced defect state would make the model extra complex.

To substantiate the findings that the interface recombination velocity is lowered by 2 and 3 orders of magnitude when the CsFAMA/C_{60} and CsFAMA/CCl/C_{60} films are cooled to cryogenic temperatures, we performed absolute ss-PL spectroscopy to determine the Q_e^{PL} as function of temperature. As discussed before, the neat CsFAMA film becomes less defective because the Q_e^{PL} increases from 9.9×10^{-3} to 2.2×10^{-1} [Fig. 4(c)]. However, for the CsFAMA/C_{60} bilayer, the gain in Q_e^{PL} is higher between room temperature and 90 K, increasing by 2 orders of magnitude from 2.1×10^{-4} to 1.7×10^{-2}, and approaching the Q_e^{PL} of the neat CsFAMA film without an ETL. This rise in Q_e^{PL} coincides with the reduction in interface recombination velocity S_{int} observed in the low-temperature tr-PL. So not only is the CsFAMA semiconductor becoming less defective, but the interfacial nonradiative losses in the CsFAMA/C_{60} film also vanish, resulting in an even greater Q_e^{PL} enhancement. For the CsFAMA films with CCl surface treatment, a similar Q_e^{PL} enhancement from room temperature to 90 K was observed as in the neat

CsFAMA film, albeit with a marginally higher Q_e^{PL} at 90 K of 4.5×10^{-1}. This is in line with the tr-PL decays, which also showed minimal changes and virtually identical shallow defect energies and densities. The Q_e^{PL} of the CsFAMA/CCl/C_{60} film also increased from 1.8×10^{-3} to 6.5×10^{-2}. Due to the passivating effect of CCl, the Q_e^{PL} at room temperature is already higher than the CsFAMA/C_{60} film, mainly due to a reduced interfacial recombination velocity S_{int} [Fig. 4(b)]. So, when the temperature is reduced, the enhancement in Q_e^{PL} lies between the CsFAMA/CCl and the CsFAMA/C_{60} films. For all these CsFAMA films, the ΔE_F increased when cooled from 300 to 100 K and started to converge at 100 K, approaching the detailed-balance limit, similar to the temperature dependence of the ΔE_F described in Eq. (2) (Fig. S22 in Supplemental Material [25]). These results show that the CsFAMA semiconductor becomes less defective when cooled to cryogenic temperatures due to thermally activated (shallow) defect formation. Moreover, the interface recombination velocity in CsFAMA/CTL bilayers is reduced between 300 and 130 K, resulting in an additional reduction of nonradiative losses, allowing the CsFAMA stack to approach the radiative limits.

III. CONCLUSIONS

In summary, using temperature-dependent tr-PL on a triple-cation perovskite (CsFAMA) film, we have demonstrated that the energetic landscape of shallow defects in CsFAMA changes between 300 and 90 K. From fitting the tr-PL traces to a model with three shallow defects, we find that these defects are thermally activated as they become shallower and vanish into the valence or conduction band at 90 K, making CsFAMA less defective. This is corroborated by the enhanced Q_e^{PL} when cooling from 300 to 100 K. We extended the temperature-dependent tr-PL method to CsFAMA films with passivation and electron transport layers on the top surface: CCl, C_{60}, and CCl/C_{60}. We find that at room temperature, the PL decay times vary across the different surface depositions due to nonradiative recombination. Treating CsFAMA with CCl does not alter the shallow-defect properties and results in identical nonradiative recombination and PL decay compared to that of the neat perovskite across all temperatures, suggesting it has no impact on the defects. Lowering the temperature for the CsFAMA/ETL stacks makes the tr-PL decay dynamics almost identical for each case, showing that nonradiative recombination losses become less dominant at low temperatures due to a reduced interface recombination velocity, as concluded from fitting the tr-PL decay. Our results provide new insight into shallow defects and charge recombination at reduced temperatures and can help us better understand the effect of surface treatments on shallow-defect properties.

ACKNOWLEDGMENTS

The authors acknowledge funding from the Dutch Research Council (NWO) (Spinoza grant), the European Union's Horizon Europe Research and Innovation Programme (LUMINOSITY, Grant Agreement No. 101147653), and the European Research Council (PERSTACK, Grant Agreement No. 101098168). G. J. W. A. fabricated the samples, measured the tr-PL, and performed the analysis. S. V. Q. M., S. M. C., and W. H. M. R measured (low temperature) absolute PL. G. J. W. A. wrote the manuscript with input from all coauthors. M. M. W. and R. A. J. J. supervised the project.

DATA AVAILABILITY

The data of the figures in this article and MATLAB scripts used for fitting and simulated tr-PL are openly available [55].

[1] J. Warby *et al.*, *Understanding performance limiting interfacial recombination in pin perovskite solar cells*, Adv. Energy Mater. **12**, 2103567 (2022).

[2] B. T. van Gorkom, T. P. A. van der Pol, K. Datta, M. M. Wienk, and R. A. J. Janssen, *Revealing defective interfaces in perovskite solar cells from highly sensitive sub-bandgap photocurrent spectroscopy using optical cavities*, Nat. Commun. **13**, 349 (2022).

[3] W. Shockley and W. T. Read, *Statistics of the recombinations of holes and electrons*, Phys. Rev. **87**, 835 (1952).

[4] D. Luo, R. Su, W. Zhang, Q. Gong, and R. Zhu, *Minimizing non-radiative recombination losses in perovskite solar cells*, Nat. Rev. Mater. **5**, 44 (2020).

[5] G. J. W. Aalbers, T. P. A. van der Pol, K. Datta, W. H. M. Remmerswaal, M. M. Wienk, and R. A. J. Janssen, *Effect of sub-bandgap defects on radiative and non-radiative open-circuit voltage losses in perovskite solar cells*, Nat. Commun. **15**, 1276 (2024).

[6] F. De Angelis and A. Petrozza, *Clues from defect photochemistry*, Nat. Mater. **17**, 383 (2018).

[7] W.-J. Yin, J.-H. Yang, J. Kang, Y. Yan, and S.-H. Wei, *Halide perovskite materials for solar cells: a theoretical review*, J. Mater. Chem. A **3**, 8926 (2015).

[8] E. Aydin, M. De Bastiani, and S. De Wolf, *Defect and contact passivation for perovskite solar cells*, Adv. Mater. **31**, 1900428 (2019).

[9] Y. Yuan, G. Yan, C. Dreessen, T. Rudolph, M. Hülsbeck, B. Klingebiel, J. Ye, U. Rau, and T. Kirchartz, *Shallow defects and variable photoluminescence decay times up to* 280 µs *in triple-cation perovskites*, Nat. Mater. **23**, 391 (2024).

[10] Y. Yuan, G. Yan, C. Dreessen, and T. Kirchartz, *Understanding power-law photoluminescence decays and bimolecular recombination in lead-halide perovskites*, Adv. Energy Mater. **15**, 2403279 (2025).

[11] W. H. M. Remmerswaal, B. T. van Gorkom, D. Zhang, M. M. Wienk, and R. A. J. Janssen, *Quantifying non-radiative recombination in passivated wide-bandgap metal*

halide perovskites using absolute photoluminescence spectroscopy, Adv. Energy Mater. **14**, 2303664 (2024).

[12] P. Caprioglio, M. Stolterfoht, C. M. Wolff, T. Unold, B. Rech, S. Albrecht, and D. Neher, *On the relation between the open-circuit voltage and quasi-Fermi level splitting in efficient perovskite solar cells*, Adv. Energy Mater. **9**, 1901631 (2019).

[13] M. Stolterfoht *et al.*, *How to quantify the efficiency potential of neat perovskite films: Perovskite semiconductors with an implied efficiency exceeding 28%*, Adv. Mater. **32**, 2000080 (2020).

[14] A. Al-Ashouri *et al.*, *Monolithic perovskite/silicon tandem solar cell with >29% efficiency by enhanced hole extraction*, Science **370**, 1300 (2020).

[15] M. Stolterfoht *et al.*, *Visualization and suppression of interfacial recombination for high-efficiency large-area pin perovskite solar cells*, Nat. Energy **3**, 847 (2018).

[16] J. Wang, V. Zardetto, K. Datta, D. Zhang, M. M. Wienk, and R. A. J. Janssen, *16.8% monolithic all-perovskite triple-junction solar cells via a universal two-step solution process*, Nat. Commun. **11**, 5254 (2020).

[17] X. Zheng, B. Chen, J. Dai, Y. Fang, Y. Bai, Y. Lin, H. Wei, X. C. Zeng, and J. Huang, *Defect passivation in hybrid perovskite solar cells using quaternary ammonium halide anions and cations*, Nat. Energy **2**, 17102 (2017).

[18] C. Liu *et al.*, *Bimolecularly passivated interface enables efficient and stable inverted perovskite solar cells*, Science **382**, 810 (2023).

[19] B. T. van Gorkom, S. H. W. Fun, T. P. A. van der Pol, W. H. M. Remmerswaal, G. J. W. Aalbers, M. M. Wienk, and R. A. J. Janssen, *Identifying the nature and location of defects in n–i–p perovskite cells with highly sensitive Sub-bandgap photocurrent spectroscopy*, Sol. RRL **8**, 2400316 (2024).

[20] H. Xie *et al.*, *Decoupling the effects of defects on efficiency and stability through phosphonates in stable halide perovskite solar cells*, Joule **5**, 1246 (2021).

[21] L. Bellini, D. Grosfeld, B. Branco, G. J. W. Aalbers, L. M. Kessels, W. H. M. Remmerswaal, N. Daub, K. Datta, M. M. Wienk, and R. A. J. Janssen, *Reducing open-circuit voltage losses in wide-bandgap* $FAPbBr_3$ *perovskite solar cells for continuous unassisted light-driven water splitting*, Adv. Funct. Mater. **36**, e17729 (2025).

[22] X. Zhu *et al.*, *Constructing Ultra-shallow near-edge states for efficient and stable perovskite solar cells*, Adv. Mater. **36**, 2309487 (2024).

[23] Y. Li, Z. Jia, Y. Yang, F. Yao, Y. Liu, and Q. Lin, *Shallow traps-induced ultra-long lifetime of metal halide perovskites probed with light-biased time-resolved microwave conductivity*, Appl. Phys. Rev. **10**, 011406 (2023).

[24] G. J. W. Aalbers, W. H. M. Remmerswaal, R. H. C. van den Heuvel, L. Bellini, L. M. Kessels, C. H. L. Weijtens, N. R. M. Schipper, M. M. Wienk, and R. A. J. Janssen, *Functionalized substrates for reduced nonradiative recombination in metal-halide perovskites*, J. Phys. Chem. Lett. **16**, 372 (2025).

[25] See Supplemental Material at http://link.aps.org/supplemental/10.1103/jzjm-xw3v for information about the experimental methods, supplemental figures, tables, and notes. It also includes Refs. [4,9,26–28].

[26] J. E. Lee, S. G. Motti, R. D. J. Oliver, S. Yan, H. J. Snaith, M. B. Johnston, and L. M. Herz, *Unraveling loss mechanisms arising from energy-level misalignment between metal halide perovskites and hole transport layers*, Adv. Funct. Mater. **34**, 2401052 (2024).

[27] S. Siebentritt, T. P. Weiss, M. Sood, M. H. Wolter, A. Lomuscio, and O. Ramirez, *How photoluminescence can predict the efficiency of solar cells*, J. Phys. Mater. **4**, 042010 (2021).

[28] J. Mooney and P. Kambhampati, *Get the basics right: Jacobian conversion of wavelength and energy scales for quantitative analysis of emission spectra*, J. Phys. Chem. Lett. **4**, 3316 (2013).

[29] C. Tao *et al.*, *Indirect bandgap emission of the metal halide perovskite* $FAPbI_3$ *at low temperatures*, J. Phys. Chem. Lett. **14**, 3805 (2023).

[30] G. Liu, M. Ghasemi, Q. Wei, B. Jia, Y. Yang, and X. Wen, *Dynamic defect tolerance in metal halide perovskites: From phenomena to mechanism*, Adv. Energy Mater. **15**, 2405239 (2025).

[31] M. van der Laan *et al.*, *Photon recycling in* $CsPbBr_3$ *all-inorganic perovskite nanocrystals*, ACS Photonics **8**, 3201 (2021).

[32] J. Wang, N. Chen, W. Wang, Z. Li, B. Huang, Y. Yang, and Q. Yuan, *Room-temperature persistent luminescence in metal halide perovskite nanocrystals for solar-driven* CO_2 *bioreduction*, CCS Chem. **5**, 164 (2022).

[33] A. Marunchenko, J. Kumar, A. Kiligaridis, D. Tatarinov, A. Pushkarev, Y. Vaynzof, and I. G. Scheblykin, *Memlumor: A luminescent memory device for energy-efficient photonic neuromorphic computing*, ACS Energy Lett. **9**, 2075 (2024).

[34] L. Krückemeier, B. Krogmeier, Z. Liu, U. Rau, and T. Kirchartz, *Understanding transient photoluminescence in halide perovskite layer stacks and solar cells*, Adv. Energy Mater. **11**, 2003489 (2021).

[35] L. Krückemeier, Z. Liu, B. Krogmeier, U. Rau, and T. Kirchartz, *Consistent interpretation of electrical and optical transients in halide perovskite layers and solar cells*, Adv. Energy Mater. **11**, 2102290 (2021).

[36] F. Peña-Camargo *et al.*, *Revealing the doping density in perovskite solar cells and its impact on device performance*, Appl. Phys. Rev. **9**, 021409 (2022).

[37] F. Ruf, M. F. Aygüler, N. Giesbrecht, B. Rendenbach, A. Magin, P. Docampo, H. Kalt, and M. Hetterich, *Temperature-dependent studies of exciton binding energy and phase-transition suppression in* $(Cs, FA, MA)Pb(I, br)_3$ *perovskites*, APL Mater. **7**, 031113 (2019).

[38] S. D. Stranks, V. M. Burlakov, T. Leijtens, J. M. Ball, A. Goriely, and H. J. Snaith, *Recombination kinetics in organic-inorganic perovskites: Excitons, free charge, and subgap states*, Phys. Rev. Appl. **2**, 034007 (2014).

[39] R. L. Milot, G. E. Eperon, H. J. Snaith, M. B. Johnston, and L. M. Herz, *Temperature-dependent charge-carrier dynamics in* $CH_3NH_3PbI_3$ *perovskite thin films*, Adv. Funct. Mater. **25**, 6218 (2015).

[40] A. M. Ulatowski, K. A. Elmestekawy, J. B. Patel, N. K. Noel, S. Yan, H. Kraus, P. G. Huggard, M. B. Johnston, and L. M. Herz, *Contrasting charge-carrier dynamics across key metal-halide perovskite compositions through in situ*

simultaneous probes, Adv. Funct. Mater. **33**, 2305283 (2023).

[41] J. Zhao, X. Liu, Z. Wu, B. Ibrahim, J. Thieme, G. Brocks, S. Tao, L. J. Bannenberg, and T. J. Savenije, *Temperature-dependent interplay between structural and charge carrier dynamics in CsMAFA-based perovskites*, Adv. Funct. Mater. **34**, 2311727 (2024).

[42] M. J. Trimpl, A. D. Wright, K. Schutt, L. R. V. Buizza, Z. Wang, M. B. Johnston, H. J. Snaith, P. Müller-Buschbaum, and L. M. Herz, *Charge-carrier trapping and radiative recombination in metal halide perovskite semiconductors*, Adv. Funct. Mater. **30**, 2004312 (2020).

[43] T. Kirchartz and U. Rau, *What makes a good solar cell?*, Adv. Energy Mater. **8**, 1703385 (2018).

[44] T. Kirchartz, J. A. Márquez, M. Stolterfoht, and T. Unold, *Photoluminescence-based characterization of halide perovskites for photovoltaics*, Adv. Energy Mater. **10**, 1904134 (2020).

[45] Z. Guo, M. Yuan, G. Chen, F. Liu, R. Lu, and W.-J. Yin, *Understanding defects in perovskite solar cells through computation: Current knowledge and future challenge*, Adv. Sci. **11**, 2305799 (2024).

[46] Y. Chen *et al.*, *Self-elimination of intrinsic defects improves the low-temperature performance of perovskite photovoltaics*, Joule **4**, 1961 (2020).

[47] J. Zhao, L. M. van der Poll, S. L. Looman, J. Yan, J. Thieme, B. Ibrahim, and T. J. Savenije, *Long-lived charge extraction in CsMAFA-based perovskites in n-i-p and p-i-n structures*, ACS Energy Lett. **9**, 2456 (2024).

[48] E. Butler-Caddle, K. D. G. I. Jayawardena, A. Wijesekara, R. L. Milot, and J. Lloyd-Hughes, *Distinguishing carrier transport and interfacial recombination at perovskite/transport-layer interfaces using ultrafast spectroscopy and numerical simulation*, Phys. Rev. Appl. **22**, 024013 (2024).

[49] J. Liu *et al.*, *Efficient and stable perovskite-silicon tandem solar cells through contact displacement by MgF_x*, Science **377**, 302 (2022).

[50] A. A. Said *et al.*, *Sublimed C60 for efficient and repeatable perovskite-based solar cells*, Nat. Commun. **15**, 708 (2024).

[51] S. C. Gillespie, J. Gautier, J. S. van der Burgt, J. Anker, B. L. J. Geerligs, G. Coletti, and E. C. Garnett, *Silicon-inspired analysis of interfacial recombination in perovskite photovoltaics*, Adv. Energy Mater. **2400965** (2024).

[52] L. Krückemeier, Z. Liu, T. Kirchartz, and U. Rau, *Quantifying charge extraction and recombination using the rise and decay of the transient photovoltage of perovskite solar cells*, Adv. Mater. **35**, 2300872 (2023).

[53] S. Akel, Y. Wang, G. Yan, U. Rau, and T. Kirchartz, *Charge carrier collection losses in lead-halide perovskite solar cells*, Adv. Energy Mater. **14**, 2401800 (2024).

[54] R. Gundermann, G. He, C. Penschke, E. Radicchi, E. Mosconi, F. D. Angelis, D. Neher, and F. Lang, *Performance Limiting Defect Stabilization by Orbital Hybridization in Perovskite/C_{60} Based Solar Cells*, EES Sol. **2**, 448 (2026).

[55] G. J. W. Aalbers, S. V. Quiroz Monnens, S. M. Calis, W. H. M. Remmerswaal, M. M. Wienk, and R. A. J. Janssen, *Supporting data for "Low Temperatures Reduce Shallow Defect Energies and Interfacial Recombination Losses in Triple-Cation Lead-Halide Perovskites"*, Zenodo, https://zenodo.org/records/20687703 (2026).